This is a remarkable paper, truly a seminal paper. It is arguably the first paper on micromachined accelerometers. It is also comprehensive: it discusses a novel design, clever fabrication, insightful analysis, prudent optimization, careful testing, and economical packaging. It pays attention to or makes passing references to sensitivity, cross-axis, sensitivity, bandwidth, range, linearity, material selection, damping, dynamic behavior, noise, drift, temperature compensation, batch-fabrication, and cost. One will be surprised today that many papers that followed this do not pay attention to all these aspects. For instance, very few papers account for the anisotropic material properties. Maximum stress due to all components of accelerations, both intended and unintended, is often not mentioned in many other papers that came after this. Attention to detail that we see in this paper is astounding.

This paper was based on a PhD thesis submitted to Stanford University, USA, in 1977. The paper appeared in 1979. As there do not seem to be any other papers by these authors (the student Roylance and the adviser Angell) on this topic, the paper also shows the good old ethic of publishing truly archival material and doing that in a concise publication. This paper has only seven pages and packs so much information and insight.

Read it carefully and try to understand every bit of it. I highlighted a few parts in yellow but I really would like to highlight the entire paper! Note also that the content of the paper and the references it cited indicate the important role mechanics plays in microsystems technology.

—G. K. Ananthasuresh, IISc, Bangalore

(for ME 237/NE 211 course students in August, 2014)

A Batch-Fabricated Silicon Accelerometer

LYNN MICHELLE ROYLANCE, MEMBER, IEEE, AND JAMES B. ANGELL, FELLOW, IEEE

Abstract—An extremely small batch-fabricatable accelerometer has been developed using silicon IC technology. The device, 3 mm long and weighing 0.02 g, is a simple cantilevered beam and mass structure sealed into a silicon and glass package. The fabrication of the accelerometer is described, and the theory behind its operation developed. Experimental results on sensitivity, frequency response, and linearity are presented and found to agree with theory. The accelerometer is capable of measuring accelerations from 0.001 to 50 *g* over a 100-Hz bandwidth, while readily implemented geometry changes allow these performance characteristics to be varied over a wide range to meet the needs of differing applications.

I. Introduction

INTEGRATED-CIRCUIT (IC) fabrication technology has permitted the development of an accelerometer weighing less than 0.02 g, in a 2 × 3 × 0.6-mm package. The accelerometer will detect accelerations down to 0.01 *g* over a 100-Hz bandwidth, with an upper acceleration limit of 50 *g*. These characteristics make the accelerometer ideal for applications requiring a very small and light transducer. Further, the versatile design allows the range to be varied readily over several orders of magnitude. The given limits meet the requirements of the biomedical applications such as measurement of heart wall motion for which the accelerometer was initially developed.

The goal of this work was to develop a transducer which meets the following specifications: 1) small size and mass; 2) sensitivity to accelerations as low as one-hundredth of the acceleration of gravity; 3) a bandwidth of 100 Hz; 4) an output stable over the limited range of temperatures encountered in biological environments; 5) an inert package; 6) an accuracy of around 1 percent; and 7) an output which is linear with acceleration. The device should be sensitive to only one component of acceleration.

II. Accelerometer Structure

The accelerometer is a glass-silicon-glass sandwich; the details of this three-layer composition are shown in Fig. 1. The center layer is the heart of the device, a very thin silicon cantilevered beam surrounded by a 200-μm-thick rim. This rim provides a rigid support for one end of the beam, a region for contact pads, and mounting surfaces parallel to the plane of the beam. The beam widens at its free end into a rectangular paddle which supports a mass, either of some dense substance such as gold or of silicon. Fig. 2, a scanning-electron micrograph of the bottom side of the silicon element, clearly shows

Manuscript received May 22, 1979; revised July 30, 1979.

L. M. Roylance was with the Integrated Circuits Laboratory, Stanford University, Stanford, CA 94305. She is now with Hewlett-Packard Laboratories, Palo Alto, CA 94304.

J. B. Angell is with the Department of Electrical Engineering, Stanford University, Stanford, CA 94305.

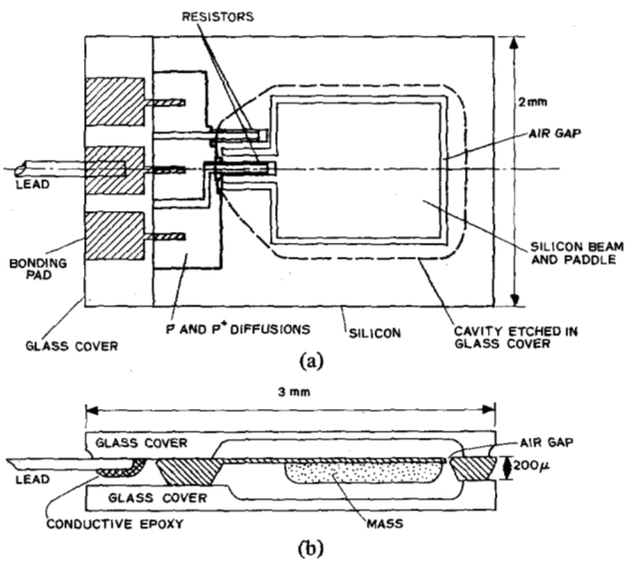

Fig. 1. Top and cross-section views of the accelerometer. (a) Top view. (b) Centerline cross section.

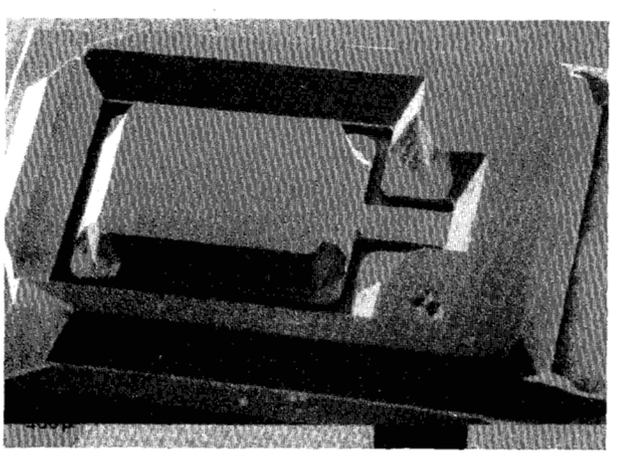

Fig. 2. SEM of backside of the accelerometer with a silicon mass after KOH etch.

the supporting rim, thin silicon beam, and integral silicon mass. A resistive half-bridge composed of two p-type resistors, one centered on the top surface of the beam and the other placed in an unstressed region of the rim, and three large p^+ contact regions complete the silicon portion of the accelerometer. The beam resistor changes its value with acceleration due to the stress induced in the beam, while the second resistor is used for temperature compensation.

The top and bottom layers, both of glass, take the place of the TO-5 can or dual-in-line package used for standard IC's. A well etched into each glass cover allows the beam to deflect

0018-9383/79/1200-1911$00.75

freely up to a given distance—and hence acceleration—set by the depth of the wells. The glass covers are hermetically sealed to the thick silicon rim using anodic bonding [1], protecting the diffusions and, by creating a sealed cavity enclosing the fragile beam and mass, the cantilever. Three narrow fingers extending from metal pads on the top glass make contact to the resistors through p^+ diffusions. A cable leading to an amplifier and recorder can be attached to these pads where the top glass overhangs the silicon. With a nonconductive epoxy filling the region between the two glass covers and around the leads, the pad region is sealed and lead bond strength improved.

III. Fabrication

Fabrication of the accelerometer is a batch process utilizing standard IC photolithographic and diffusion techniques in addition to the special etching techniques required to shape the silicon and glass. The silicon element and the top and bottom glass covers are fabricated separately in wafer form and then bonded together. The final steps are die separation and lead attachment.

The starting material is n-type (100) silicon, chosen because the preferred ⟨110⟩ direction for p-type piezoresistors coincides with the pattern orientation of anisotropic etchants such as KOH in silicon. Precise dimensional control can be obtained even with a large etch depth since the {111} planes are etched two orders of magnitude more slowly than {100} and {110} surfaces. The first step is to etch half a dozen widely spaced alignment holes completely through the wafer to obtain proper registration of patterns on the top and bottom surfaces. A 1.5-μm thermal oxide is grown and two photolithographies and diffusions done to form the 10 $\Omega/\square$ p^+ contacts and the 100 $\Omega/\square$ p resistors. The front oxide is stripped before drive-in to minimize surface steps, while the back oxide is preserved as the final etch mask. The remaining processing steps all concern the shaping of the beam, silicon mass (if present), scribe lines, and the window where the glass overhangs the silicon.

Using a thick densified layer of deposited silicon dioxide to protect the front, windows are opened in the backside oxide and the silicon is etched away around the beam and mass and in the region where the beam is to be thinned. The etch is stopped when the beam region is twice the desired final thickness. The sequence of operations is sketched in Fig. 3. A photolithography on the top surface of the partially etched wafer defines the air gap around the beam and the window opening. The final KOH etch, which etches the beam from the bottom and the air-gap regions from both top and bottom, is quenched the moment the silicon disappears from the large window openings. This visual endpoint gives very good control of the beam thickness provided the front and back surfaces of the wafer are parallel. Observed uniformity has been very good. The final step is stripping the remaining oxide.

The glass cover plates are also prepared in wafer form, from 200-μm-thick pieces of #7740 Pyrex glass, polished optically flat on one side. The type of glass is dictated by the silicon–glass bonding process which requires a glass which is slightly conductive at the bonding temperature and whose thermal expansion coefficient matches that of silicon. Unfortunately, this glass is not nearly as easy to etch as is silicon. Wells are etched in the top and bottom glass covers with a 30-percent

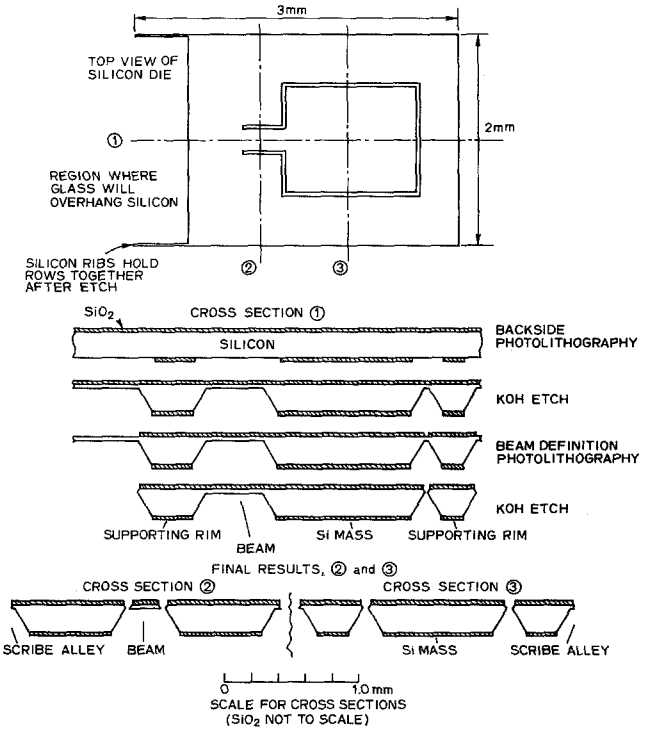

Fig. 3. Diagram of final etch steps.

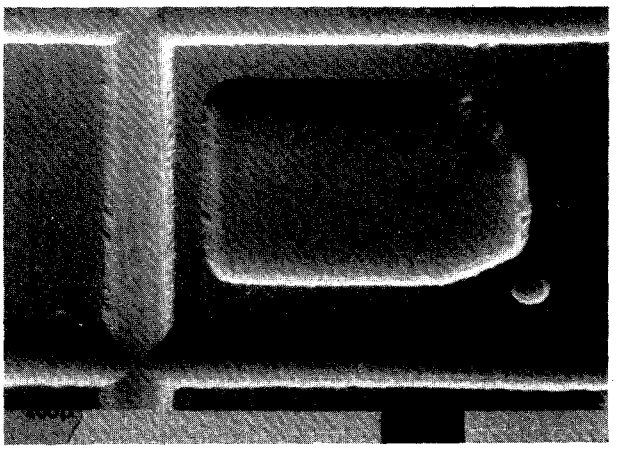

Fig. 4. SEM of top glass cover.

HNO_3, 70-percent HF mixture at 48°C and a chrome-gold etch mask. This procedure was found to give smooth, consistent results with minimal undercutting (Fig. 4). Once the masking layer is stripped, aluminum is deposited on the top glass and the metal bonding pads defined.

Final assembly of the accelerometer sandwich involves attaching gold masses if needed, and aligning and bonding the glass covers to the silicon. Only after completion of the bonding process are the individual accelerometers broken apart and handled one by one through the final phases—attaching a cable suited to the proposed application and applying insulation or some other protective coating. The heart of the assembly procedure is the anodic bonding technique which produces a hermetic and irreversible seal between silicon and glass. The glass and silicon are aligned, the temperature raised to about 400°C, and 600 V applied between the silicon and the glass. An advantage of this technique, in addition to its simplicity

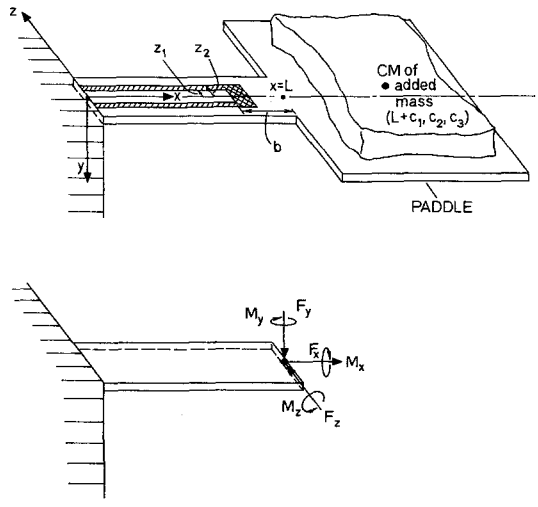

Fig. 5. Cantilevered beam and mass, with diagram of equivalent loads.

and lack of filler or "glue," is the visual inspection possible for a successful bond. Bonded areas appear dark gray, while unbonded regions are much lighter in color and show interference fringing. With the top and then bottom covers bonded, a dicing saw is used to separate the individual devices and leads are attached.

IV. Analysis

Static Response

A detailed analysis [2] (see Appendix) of the accelerometer structure shown in Fig. 5 gives the fractional resistance change of the accelerometer due to an acceleration a_y

$$\frac{\Delta R}{R} = \left\{\left[\frac{1}{2}(\Pi_{11} + \Pi_{12} + \Pi_{44}) - \left(s_{12} + \frac{1}{2}s_{44}\right)\right] \cdot \left[M\left(c_1 + \frac{L+b}{2}\right)\frac{c-h}{\mathcal{I}_z}\right]\right\} a_y = S_0 a_y \tag{1}$$

where L and h are the beam length and thickness, $\mathcal{I}_z$ the moment of inertia of the beam cross section about the z axis, c the distance from the centroid of the cross section to the bottom of the beam, M the mass loading the beam with its center of gravity at $(L + c_1, c_2, c_3)$, and Π_{ij} and s_{ij} the piezoresistive and elastic compliance coefficients referred to the cubic axes of silicon. The resistor extends from $x = 0$ to $x = L - b$. The accelerometer's sensitivity shows the desired linearity; further, the magnitude of the response can readily be controlled by varying the geometry.

Ideally (1) is the only term present for any acceleration a. The structure's effectiveness as a uniaxial accelerometer can be assessed by comparing the magnitudes of the responses to a_x and a_z with the desired sensitivity S_0. The only nonzero terms are due to the axial force F_x and the moment M_z produced by a_x

$$\frac{\Delta R/R\,|_{a_x}}{\Delta R/R\,|_{a_y}} \simeq \left\{\frac{h}{12\,(2c_1 + L + b)} - \frac{2c_2}{2c_1 + L + b}\right\}\frac{a_x}{a_y}. \tag{2}$$

The approximation assumes $h \ll w$, where w is the width of the beam. Clearly, an effort must be made to place the mass symmetrically ($c_2 \ll 2c_1 + L + b$) and to ensure that the beam thickness is small compared to its overall length if axial accelerations are to be ignored.

In deriving the foregoing results, a massless beam and perfect alignment centering the resistor and orienting it along a 110 direction were assumed. However, for the alignment tolerances and beam dimensions of interest the combined error involved is less than 1 percent worst case [3]. In addition, the added bending of a deflected beam due to an axial load can produce another undesired output term. However, calculations of the combined effects of such axial and lateral loads show that the error term is less than 0.4 percent for an axial load equal to 1 percent of the Euler load. For a thin beam and heavy mass (worst case), this loading is roughly equal to the safe operating range of the device.

In summary, the conditions necessary to minimize the undesirable responses to a_x and a_z are

$$h, c_2 \ll 2c_1 + L + b \qquad |z_r| \ll |h - c|$$
$$h \ll w \qquad \alpha_m \ll 1 \text{ rad} \tag{3}$$

where α_m and z_r are the angular and linear misalignments of the resistor. Similarly, the criterion for a large response to a_y can be expressed as

$$3M(2c_1 + L + b) \gg wh^2. \tag{4}$$

Since this condition is compatible with the constraints (3), the accelerometer design meets the criteria for a sensitive, uniaxial device whose response to a given acceleration can be both closely controlled and tailored to a particular task.

Dynamic Behavior

The primary purpose of this accelerometer is to measure time-varying accelerations, requiring an understanding of the variation in its behavior with the frequency of the excitation. For very low frequencies, the beam can follow the excitation without appreciable delay, so the discussion of the accelerometer's static response is directly applicable. At higher frequencies, however, the dynamic characteristics of the system produce phase delays and amplitude variations, depending on the natural frequencies of the device. A high-Q resonance (in an undamped accelerometer) corresponding to the first mode of lateral vibration of the beam dominates the behavior of the accelerometer. The other vibrational modes of the beam occur at much higher frequencies. Hence, the motion of the cantilevered beam and mass can be modeled as a simple two-pole spring and mass system.

The deflection of the beam is very nearly the deflection of a massless beam with a rigid distributed mass M at its end. For a static load F_y acting on the centroid of M, the deflection can be written as [4]

$$y = \begin{cases} \dfrac{F_y x^2}{2E\mathcal{I}_z}\left(L - \dfrac{x}{3} + c_1\right), & 0 \leqslant x \leqslant L \\ \dfrac{F_y L^2}{2E\mathcal{I}_z}\left(\dfrac{2}{3}L + c_1\right) + \left[\dfrac{F_y L^2}{2E\mathcal{I}_z} + \dfrac{F_y c_1 L}{E\mathcal{I}_z}\right](x - L), & L < x \leqslant L + 2c_1 \end{cases} \tag{5}$$

where E is Young's Modulus. Note that the restoring force

(F_y) on the mass M is proportional to its displacement, giving simple harmonic motion. Applying the Rayleigh principle [5] to this deflection curve, a very good approximation to the resonant frequency ω_n is obtained (for M uniformly distributed)

$$\omega_n \simeq \sqrt{\frac{E\mathfrak{I}_z}{ML^3}\,\frac{2+6f+f^2}{\frac{2}{3}+4f+\frac{21}{2}f^2+14f^3+8f^4}} \tag{6}$$

where the second factor under the radical varies from three to one-tenth as $f = c_1/L$ varies between zero and two. Note that the key parameters affecting ω_n also play a large role in determining the sensitivity. This interrelationship limits the bandwidth which can be obtained for a given sensitivity. For typical accelerometer designs, ω_n is between 500 Hz and 5 kHz; the analysis of the preceding section is, therefore, valid over the 100-Hz bandwidth of interest.

Optimization

We now have the tools to explore the capabilities and limitations of this miniature accelerometer. Expressions for the dependence of the sensitivity, resonant frequency, and deflection of the accelerometer on its geometric and materials parameters have been developed which apply, in fact, to any accelerometer design consisting of a uniform cantilevered beam, a mass, and a stress-sensitive element to detect the stress in the beam. Therefore, much of the following discussion applies rather generally to small accelerometers using the cantilevered structure.

Three materials parameters, the magnitude of the piezoresistive coefficients in silicon, the density of the mass, and the fracture stress of silicon, set fundamental limits on the performance. In particular the relationship between the maximum stress in the beam and the applied acceleration places an upper limit on the sensitivity

$$S_0\Big|_{\max} = \frac{\Pi_{\text{eff}}}{a_r}\,\sigma_{\text{fracture}}\left[\frac{2c_1+L+b}{2(L+c_1)}\right] \simeq \Pi_{\text{eff}}\,\frac{3.5\times 10^9}{a_r} \simeq \frac{0.12}{a_r} \tag{7}$$

where a_r is the range in acceleration, σ_{fracture} the fracture stress, Π_{eff} the effective piezoresistive coefficient, and where $2c_1 >> L + b$.

The geometry of the accelerometer also has a profound effect on its performance. The most significant parameter is the beam thickness h, whose impact on sensitivity, resonant frequency, and beam deflection is plotted in Fig. 6 for typical values of h. The optimal choice for h is the smallest value consistent with the bandwidth and deflection constraints (set by the glass wells) in the design, since this choice gives both a large gain-bandwidth product and minimal transverse axis response. The minimum beam thickness, from fabrication and deflection considerations, is 5 μm. Although w and M also influence the performance, the beamwidth is set primarily by structural considerations, while the mass is a convenient way of setting the sensitivity. By selecting h and M a wide variety of accelerometers of differing ranges, sensitivities, and useful bandwidths can be built from the same basic structure. The

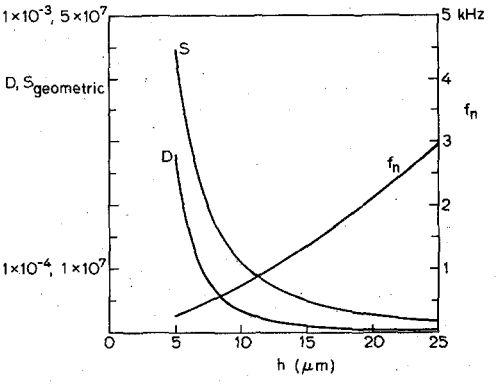

Fig. 6. Sensitivity S, resonant frequency f_n, and deflection D versus beam thickness h. Accelerometer dimensions: w = 0.02 cm, c_1 = 0.06 cm, b = 0.01 cm, M = 4.5 × 10^{-4} g (scale for S must be multiplied by Π_{eff} to obtain $\Delta R/R$).

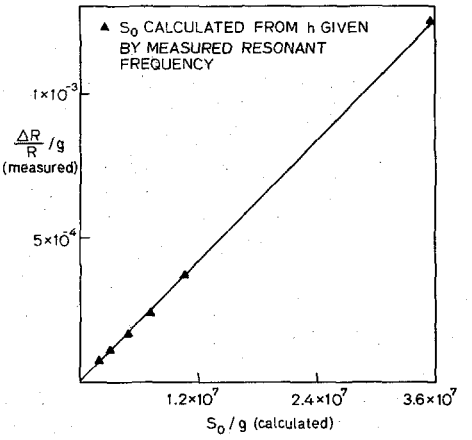

Fig. 7. Experimental versus theoretical geometric sensitivity. Slope = 3.5 × 10^{-11} cm²/dyne = Π_{eff}.

current package size allows a dynamic range of 10^4 and ranges of 1 to 10^3 g.

V. Experimental Results

The static responses of accelerometers of varying beam dimensions and masses were measured using the acceleration of gravity as a reference. By varying the orientation of the beam with respect to gravity, and comparing the outputs, the contributions of each of the three components of acceleration were determined. The observed outputs were linear in a_y and a_x, while no dependence on a_z was detected, as predicted by (1) and (2). The measured fractional resistance change due to a_y is graphed for several accelerometers in Fig. 7 against the prediction in (1), omitting the term in the piezoresistive coefficients. The points fall beautifully on a straight line through the origin with a slope of 3.5 × 10^{-11} cm²/dyne, very close to the 4.5 × 10^{-11} calculated for Π_{eff}, using published values for the piezoresistive and elastic compliance coefficients.

Turning to the most significant transverse or off-axis responses, which are plotted in Fig. 8, two of the terms, e_1 and e_3, representing the effects of axial stress and of a beam of nonzero mass, respectively, are found to be extremely small even under worst case conditions. The third, and critical, component, e_2, arises from the moment M_z due to an acceleration

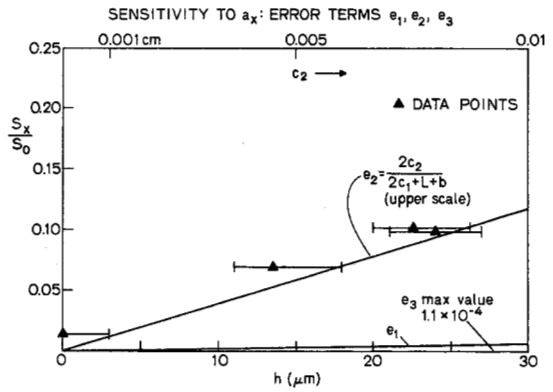

Fig. 8. Components of relative sensitivity to a_x; e_1, e_3 versus beam thickness h; e_2 versus c_2.

a_x. For a large mass mounted on one side of the paddle, this component is a substantial fraction of the y-axis sensitivity S_0, although it decreases to zero for a symmetrically mounted mass. Data from several accelerometers are plotted in Fig. 8 and show the trend predicted, although the rather large uncertainty in the magnitude of c_2 prevents assessment of the accuracy of the theory to better than about 20 percent.

To compare the two-pole model with the actual behavior of the accelerometer, the impulse responses of several accelerometers were determined experimentally.[1] Oscillograms of a typical impulse response can be found in Fig. 9. The damped sinusoidal behavior and the clean characteristics of the first few cycles indicate that the two-pole model is indeed a good choice. Values of the resonant frequency were found to agree very well with (6). Despite a factor of eighteen variation in sensitivity for the accelerometers tested, all had similar values for the damping factor ζ, Q, and the damping force F_d, corresponding to air damping of the beam plus any internal damping in the silicon. The exponential decay shown corresponds to $\zeta = 0.0046$, $Q = 109$, and $F_d = 0.065\ dy/dt$ (dynes).

Damping the beam resonance by adding a suitable fluid to the accelerometer cavity is a very attractive approach to minimize the impact of the resonance and increase the useful bandwidth. Four common laboratory fluids of roughly equal densities, acetone, methanol, deionized water, and isopropyl alcohol, were used to investigate the dependence of the accelerometer damping factor on fluid viscosity. The damping factor was found to vary linearly with fluid viscosity, as shown for one device in Fig. 10, while the viscosity needed to give 0.7 critical damping was found, by extrapolating the data points, to vary between 3 and 4 centipoise depending on the device. Some of the silicone oils have viscosities of this magnitude, and may well prove attractive to damp the accelerometer.

Damping the accelerometer will make it less susceptible to small fluctuations in ambient temperature, due to the increase in thermal mass, and may also help maintain the two resistors at the same temperature, both desirable effects. However, the

[1] The accelerometer was mounted on one face of a short piece of drill rod used as the weight for one pendulum of a dual-pendulum arrangement. A steel sphere weighting the other pendulum was released from a measured distance to swing into the opposite face of the rod; the resulting impact is an impulse on the time scale of the accelerometer.

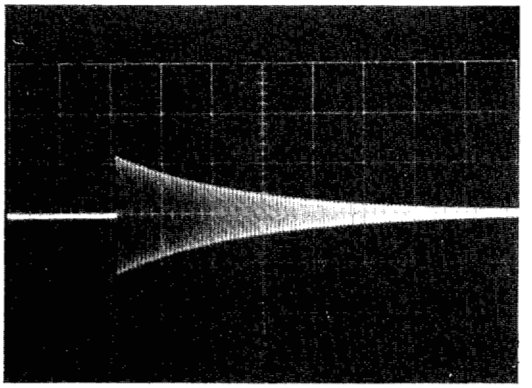

(a)

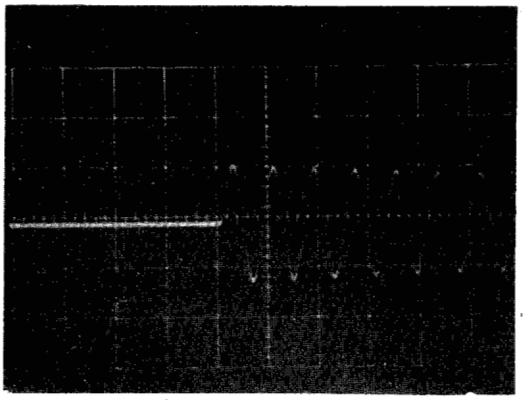

(b)

Fig. 9. Accelerometer impulse response. (a) 1 V/vert. div., 5 ms/horiz. div. (b) Same device, 1 V/vert. div., 0.5 ms/horiz. div.

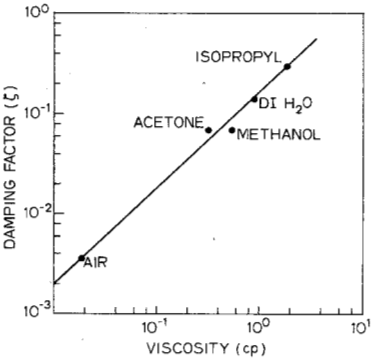

Fig. 10. Damping factor versus damping fluid viscosity.

beam and mass are totally immersed in the damping fluid, so that the buoyant force on the mass must be considered in determining the sensitivity of the damped accelerometer. In effect, the mass appearing in (1) is reduced by the mass of an equal volume of fluid. Although this change has little effect for a device with a gold mass, it can be important for a silicon mass device, particularly if the fluid density approaches the density of silicon.

Performance Limitations

Perceived accelerometer performance is affected by two inescapable properties of real systems, noise and temperature sensitivity. Thermal noise ultimately determines the useful

range of the accelerometer. Measurements made on several accelerometers indicate that the resistors contribute only Johnson noise, so that fairly conventional amplifier noise analysis and design techniques are applicable to the accelerometer. Modeling the system as a Wheatstone bridge followed by a single amplifier stage, the minimum detectable acceleration a_{min} (for signal/noise = 1), assuming a low noise amplifier and a 100-Hz bandwidth, is

$$a_{min} = \frac{1}{1.5 \times 10^8 \sqrt{P_S}\, \Delta R/R} \tag{8}$$

where P_S is the power supplied to the bridge, $\Delta R/R$ is the factional resistance change per unit acceleration of the accelerometer, and $R = 7.5$ kΩ. For the most sensitive designs a_{min} is less than 0.001 g.

The temperature dependence of the accelerometer output imposes another limitation on performance. Both the resistance differential between the sensing and temperature compensation resistors and the sensitivity $\Delta R/R$ are functions of temperature. The drift in the accelerometer output is due principally to the combination of the temperature coefficients of the diffused resistors and any mismatch between the resistors. However, since drift can be eliminated whenever it is not necessary to measure true dc acceleration, the thermal variation of accelerometer sensitivity is generally more significant. This variation is due to the temperature coefficient of the piezoresistive effect in silicon, and has been found to be between −0.2 and −0.3 percent per degree Celsius, in agreement with published values. Although this variation is not significant for the constant temperature environment of the body, for other applications both the sensitivity change and the drift can be compensated for by using more elaborate techniques on the temperature compensation resistor output.

The final concern in evaluating limitations on accelerometer performance is the linearity of the input–output characteristics. This linearity was verified experimentally by measuring outputs over the range ±1 g and peak responses to impulses of various magnitudes. Results from several accelerometers are plotted in Fig. 11 against the magnitude of the applied impulse, with the equivalent peak acceleration given for each device. The output characteristics are quite linear even though the data include points up to roughly one-fifth the acceleration at which the devices are expected to break. The nonlinearity is about ±2 percent of the maximum output, due to the bridge configuration and other sources such as the nonlinearity of the piezoresistive effect at high stress levels.

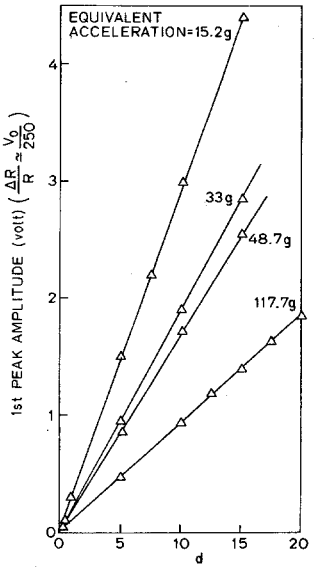

Fig. 11. Linearity of accelerometer response: impulse $\simeq 0.37\ \omega_n d$.

TABLE I
CHARACTERISTICS OF THE MINIATURE ACCELEROMETERS

Property	Silicon Mass	Gold Mass
Size	2x3x0.6mm	
Mass (of accelerometer)	0.02 gm	0.02 gm
Range	± 200 g	± 40 g
Overrange	± 600 g	±120 g
Sensitivity $\frac{\Delta R}{R}/g$	2×10^{-4}	1×10^{-3}
mV/g/V supply	0.05	0.25
Resonant Frequency	2330 Hz	1040 Hz
Transverse Sensitivity	10 %	2 %
Nonlinearity	≃ ±1% Full Scale	
Thermal Zero Shift	±1.4% FS/100°F	
Thermal Sensitivity Shift	±11%/100°F	
Resistance	7.5 kΩ	

VI. Conclusion

The purpose of this section is twofold: to summarize the key characteristics of this accelerometer, and to evaluate what has been achieved in its fabrication. The characteristics of two miniature accelerometers, one fabricated with a gold mass and the other with silicon mass, are given in Table I. They are representative of the range of devices fabricated during this investigation. Immediately apparent are the very small size and mass of both accelerometers—a major goal. Further, most of the remaining device characteristics are more than adequate for the proposed applications, and compare favorably with similar (though much larger) commercial strain gauge accelerometers. The undesirable transverse sensitivity of the silicon mass device is due solely to the asymmetric loading of the mass, and hence the cost of the miniature accelerometer comes in sensitivity and in thermal sensitivity shift. Temperature compensation of the response should reduce the thermal sensitivity shift to close to ±1 percent/100°F in applications where thermal variations are important. In addition, the sensitivity of the present design can be doubled by going to a full bridge configuration with two active elements.

This investigation has demonstrated the feasibility of an extremely small batch-fabricated accelerometer. The performance and limitations of the miniature transducer have been thoroughly explored, and an understanding developed of the importance of symmetry in the design to minimize cross-axis responses. Accelerometers with sensitivities varying from $\Delta R/R = 5 \times 10^{-5}$ to 2×10^{-3} per g have been fabricated, al-

lowing accelerations less than 0.001 g to be detected. The miniature accelerometers compare very well with the small strain gauge accelerometers available commercially, while providing more than an order of magnitude reduction in volume and mass. The small size of this accelerometer, coupled with its performance and the low cost potential of batch fabrication, makes it extremely attractive for many applications.

Appendix

Analysis of the accelerometer response to an arbitrary input can be divided into two distinct areas; one concerns the electrical output due to a given stress distribution in the silicon, while the other concerns the stress distribution which results from an arbitrary load. For a cubic crystal such as silicon and an arbitrary (′) coordinate system, the effect of stress on Ohm's Law can be written as

$$E'/\rho_0 = (1 + \Delta')\, J \tag{A1}$$

where E' and J' are the electric field and current density, respectively, ρ_0 the unstressed resistivity, and[2]

$$\Delta' = \begin{bmatrix} \Delta\rho_1'/\rho_0 \\ \Delta\rho_2'/\rho_0 \\ \Delta\rho_3'/\rho_0 \\ \Delta\rho_4'/\rho_0 \\ \Delta\rho_5'/\rho_0 \\ \Delta\rho_6'/\rho_0 \end{bmatrix} = \begin{bmatrix} \Pi_{11}' & \Pi_{12}' & \cdots & \Pi_{16}' & \sigma_1' \\ \Pi_{21}' & \cdot & & \cdot & \sigma_2' \\ \Pi_{31}' & & \cdot & \cdot & \sigma_3' \\ \Pi_{41}' & & \cdot & \cdot & \sigma_4' \\ \Pi_{51}' & & & \cdot\ \cdot & \sigma_5' \\ \Pi_{61}' & \cdot & \cdots & \Pi_{66} & \sigma_6' \end{bmatrix} \tag{A2}$$

Π_{ii}' and ρ_i' are the piezoresistive and resistivity coefficients, and σ_i' the stresses. For a resistor oriented along the 110 direction the resulting fractional resistance change is

$$\frac{\Delta R}{R} = \frac{1}{2}(\Pi_{11} + \Pi_{12} + \Pi_{44})\,\sigma_x' + \Pi_{12}\sigma_y' + \frac{1}{2}(\Pi_{11} + \Pi_{12} - \Pi_{44})\,\sigma_z' + \epsilon_x' - \epsilon_y' - \epsilon_z' \tag{A3}$$

where the σ_i' are now the tensile stresses and ϵ_i' the strains along and perpendicular to the beam and resistor. The piezoresistive coefficients are referred to the cubic axes of silicon. (In deriving (1) the strains have been expressed in terms of the stresses and the elastic compliance coefficients s_{ij}.)

The stress in the resistor as a function of acceleration can be found by an analysis of the equivalent cantilever of Fig. 5 since the resistor does not extend into the region near the transition between the beam and paddle where the actual distribution of shear and normal forces due to a load on the mass is significant [6]. Replacing these forces by their resultants, the load on the equivalent cantilever is

$$\begin{aligned} F_x &= -Ma_x & M_x &= M(c_3a_y - c_2a_z) \\ F_y &= -Ma_y & M_y &= M(c_1a_z - c_3a_x) \\ F_z &= -Ma_z & M_z &= M(c_1a_y - c_2a_x) \end{aligned} \tag{A4}$$

where a_i, F_i, and M_i are the components of the acceleration and the resultant forces and moments. Applying the general theory of mechanics [7], [8] and the principle of superposition to the accelerometer's trapezoidal cross section and cubic anisotropy, a complete solution for the tensile stress distribution and an approximate solution for the shearing stresses is obtained [2]. The tensile stress σ_x' is the only nonzero stress term appearing in (A3).

$$\sigma_x = -a_x\left[\frac{M}{A} + \frac{Mc_2}{\mathcal{I}_z}y + \frac{Mc_3}{\mathcal{I}_y}z\right] + a_y\left[\frac{M(L + c_1 - x)}{\mathcal{I}_z}y\right] + a_z\left[\frac{M(L + c_1 - x)}{\mathcal{I}_y}z\right] \tag{A5}$$

where A is the area of the beam cross section and $\mathcal{I}_i$ are the appropriate moments of inertia. The current flow in the resistor can be assumed to be confined to the surface of the beam, $y = c - h$, because of the doping profile of the diffusion. However, the stress in the beam must be averaged over the x and z excursions of the resistor to calculate the resulting fractional resistance change (1).

[2] If the cubic axes are used, all the Π_{ij} coefficients are zero except for the nine matrix elements in the upper left quadrant and the three along the lower diagonal.

References

[1] G. Wallis and D. I. Pomerantz, "Field-assisted glass-metal sealing," *J. Appl. Phys.*, vol. 40, no. 10, p. 3946, Oct. 1969.

[2] L. M. Roylance, "A miniature integrated circuit accelerometer for biomedical applications," Ph.D. dissertation, Department of Electrical Engineering, Stanford University, Stanford, CA, pp. 47–80, 1977.

[3] *Ibid.*, pp. 74–78.

[4] S. Timoshenko and D. H. Young, *Elements of Strength of Materials*, 5th ed. New York: Van Nostrand Reinhold, 1968, p. 197ff.

[5] W. T. Thomson, *Theory of Vibration with Applications*. Englewood Cliffs, NJ: Prentice-Hall, 1972, p. 200.

[6] Adhémar Jean Claude Barré de Saint-Venant, "Mémoire sur la torsion des prismes," in *Mémoires des Savants Étrangers*, vol. 14, 1885.

[7] S. Timoshenko and J. N. Goodier, *Theory of Elasticity*, 2nd. ed. New York: McGraw-Hill, 1951.

[8] S. G. Lekhnitskii, *Theory of Elasticity of an Anisotropic Elastic Body*, translated by P. Fern. San Francisco, CA: Holden-Day, 1963.